

# TerraSky3D: Multi-View Reconstructions of European Landmarks in 4K

Mattia D’Urso<sup>1</sup> Yuxi Hu<sup>1</sup> Christian Sormann<sup>2</sup>  
 Mattia Rossi<sup>2</sup> Friedrich Fraundorfer<sup>1</sup>

<sup>1</sup>Graz University of Technology {name.surname@tugraz.at} <sup>2</sup>Sony {name.surname@sony.com}



Figure 1. **Example scene from TerraSky3D.** Left: Sparse reconstruction of the Villalta Castle, Italy. Right: Representative images collected from aerial and ground perspectives, shown with their corresponding semantically filtered depth maps.

## Abstract

*Despite the growing need for data of more and more sophisticated 3D reconstruction pipelines, we can still observe a scarcity of suitable public datasets. Existing 3D datasets are either low resolution, limited to a small amount of scenes, based on images of varying quality because retrieved from the internet, or limited to specific scenarios.*

*Motivated by this lack of suitable 3D datasets, we captured TerraSky3D, a high-resolution large-scale 3D reconstruction dataset divided into 155 ground, aerial, and mixed scenes. The dataset focuses on European landmarks and comes with curated calibration data, camera poses, and depth maps. TerraSky3D tries to answer the need for challenging dataset that can be used to train and evaluate 3D reconstruction-related pipelines.*

## 1. Introduction

The robust understanding and reconstruction of 3D environments from 2D imagery remains a fundamental challenge in computer vision. Advances in downstream applications such as robotic navigation, augmented and virtual reality, and cultural heritage preservation increasingly rely on high-quality, large-scale 3D datasets to train and benchmark modern deep learning models. Specifically, methods in Structure-from-Motion (SfM), Multi-View Stereo (MVS), and neural scene representation are continuously pushing the boundaries of photorealism and geometric accuracy, driving the demand for datasets that accurately reflect real-world geometry.

Existing large-scale datasets often suffer from several limitations. Datasets built from internet photo collections [17, 27] frequently contain inconsistent image quality, unreliable camera intrinsics, and noisy geometry. Furthermore, the

majority of datasets focus exclusively on either ground-level (street view) [10, 17, 24, 27] or aerial [29, 35, 36] perspectives. This creates a significant modality gap that hinders the development of robust cross-view algorithms. The rapid adoption of unmanned aerial vehicles (UAVs) in surveying and infrastructure inspection has made the aerial perspective increasingly relevant in practical applications, yet robust models are hindered by the lack of aerial and ground training data. This limits the development of cross-view algorithms capable of understanding drastically different viewing angles and scales, a necessary capability for real-world scenarios, such as aerial and ground relocalization. Additionally, recent state-of-the-art methods such as RoMa v2 [9] demonstrate that incorporating aerial and ground data significantly improves model robustness against large viewpoint changes.

In this paper, we introduce **TerraSky3D**, a new large-scale dataset designed to address the challenges outlined above. TerraSky3D provides a comprehensive collection of diverse outdoor scene categories, primarily focused on complex European landmarks across Central and Southern Europe, as shown in Fig. 2. By leveraging a high-resolution 4K acquisition pipeline and adopting a rigorously revisited processing methodology for generating dense geometric products, we ensure geometrically consistent data for both ground-level and aerial viewpoints. The dataset includes scenes composed of only ground views, only aerial views, and, mixed aerial and ground scenes, offering extensive versatility for various research domains. Figs. 1, 3, 5, 6, 7 show some examples of the proposed scenes. Our contributions are summarized as follows.

1. **A New Large-Scale Mixed Dataset:** A novel large-scale dataset of high-resolution ground-level and aerial imagery featuring mixed scenes.
2. **A Simplified Processing Pipeline:** A modern and simplified processing methodology to convert raw video acquisitions into dense, geometrically reliable 3D reconstructions.
3. **A Comprehensive Evaluation:** A set of experiments validating our data and evaluating current state-of-the-art methods on modern acquisition data.

Find the dataset at [github.com/mattiadurso/TerraSky3D](https://github.com/mattiadurso/TerraSky3D).

## 2. Related Work

**Large-Scale Outdoor Photo Collections.** Large-scale datasets derived from unconstrained internet photos, such as MegaDepth [17] and MegaScenes [27], have significantly advanced tasks like pose estimation, visual place recognition, depth estimation, and novel view synthesis. These datasets are typically curated by collecting vast quantities of images from public internet sources, which then require extensive processing and cleaning pipelines. Both MegaDepth and MegaScenes utilize COLMAP [23] to estimate the 3D geometry. MegaDepth extends this process to dense depth es-

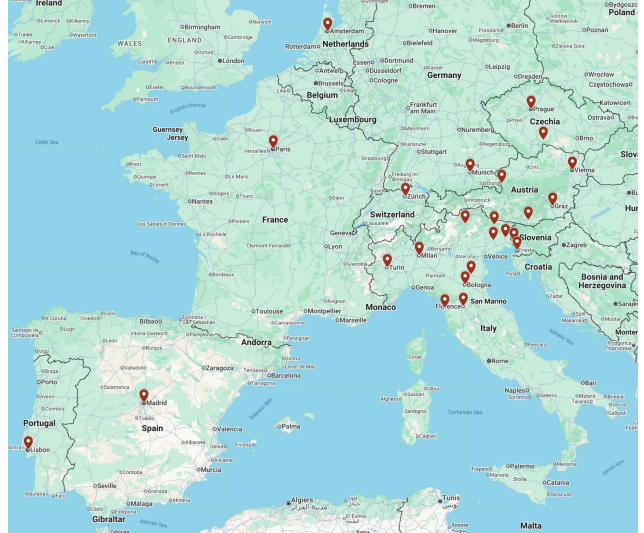


Figure 2. **Geographical Distribution of Data Collection Sites in TerraSky3D.** The dataset includes sites across 11 European countries. Close locations might share the same red pin.

timation using the COLMAP MVS pipeline, followed by post-processing steps such as depth filtering, masking, and refinement. In contrast, MegaScenes primarily provides sparse point clouds. A common challenge in both datasets is detecting and removing artifacts, such as watermarks or timestamps.

A significant limitation of these internet-sourced collections is the lack of known intrinsic camera parameters or shared camera parameters across images. Consequently, intrinsics must be estimated by COLMAP for each image, a process that is prone to inaccuracies, especially when each camera corresponds to only one image. Furthermore, these datasets often contain images with varying aspect ratios within the same scene.

TerraSky3D tackles these problems. We do not collect data from internet sources; instead, we capture each scene specifically for 3D reconstruction. This approach provides sufficient angular views for COLMAP to accurately recover both the 3D structure and the camera poses. By carefully collecting the data, we ensured all images were captured at 4K resolution with a constant aspect ratio. Furthermore, we leverage a recent method for depth estimation, employing APD-MVS [31] for depth generation. Finally, we employ Mask2Former for semantic filtering within a streamlined yet effective pipeline.

**Mixed Aerial and Ground data.** Drone imagery has become pivotal for 3D mapping and vision research, as evidenced by recent datasets [3, 16, 29, 35, 36]. However, existing datasets exhibit limitations that hinder the training of robust real-world models for this purpose. For in-

Table 1. **Comparison of MVS and 3D Reconstruction Datasets.** An  $\times$  under **Scenes** indicates that the number of scenes is not available. **Types** are G (Ground) or M (Mixed Air and Ground).  $\checkmark$  under **Real** indicates collected imagery, whereas  $\times$  denotes computer-generated images; both aerial and ground are indicated when available (e.g.,  $\times/\checkmark$  means aerial is computer-generated but ground is real). HR denotes High Resolution (Full HD or above). **Calib.** indicates camera pre-calibration ( $\checkmark$ ) or intrinsic estimation during the reconstruction process ( $\times$ ).  $\checkmark$  **COLMAP** indicates geometry estimated with COLMAP, while  $\times$  indicates no geometry is available. RC stands for Reality Capture.

| Dataset                     | Year | #Scenes  | Type | Real                    | HR           | Calib.       | COLMAP            | Depth      |
|-----------------------------|------|----------|------|-------------------------|--------------|--------------|-------------------|------------|
| MegaDepth [17]              | 2018 | 135      | G    | $\checkmark$            | $\times$     | $\times$     | $\checkmark$      | COLMAP-MVS |
| MegaScenes [27]             | 2024 | 100K     | G    | $\checkmark$            | $\times$     | $\times$     | $\checkmark$      | $\times$   |
| University-1652 [36]        | 2020 | 1652     | M    | $\times/\checkmark$     | $\times$     | $\times$     | $\checkmark$      | COLMAP-MVS |
| CVD-SfM [16]                | 2025 | 3        | M    | $\checkmark/\checkmark$ | $\checkmark$ | $\times$     | $\checkmark$ +GPS | $\times$   |
| Culture3D [35]              | 2025 | 41       | M    | $\checkmark/\checkmark$ | $\checkmark$ | $\checkmark$ | $\checkmark$ +RC  | $\times$   |
| AerialMegadepth [29]        | 2025 | 137      | M    | $\times/\checkmark$     | $\times$     | $\times$     | $\checkmark$      | COLMAP-MVS |
| Megadepth Air-to-Ground [3] | 2025 | $\times$ | M    | $\checkmark/\checkmark$ | $\times$     | $\times$     | $\checkmark$      | $\times$   |
| Tokyo 24/7 [26]             | 2015 | 125      | G    | $\checkmark$            | $\times$     | $\times$     | $\times$          | $\times$   |
| HPatches [1]                | 2017 | 116      | G    | $\checkmark$            | $\times$     | $\times$     | $\times$          | $\times$   |
| AAachen [22]                | 2018 | 1        | G    | $\checkmark$            | $\times$     | $\checkmark$ | $\checkmark$      | $\times$   |
| MegaDepth-1500 [25]         | 2018 | 2        | G    | $\checkmark$            | $\times$     | $\times$     | $\checkmark$      | COLMAP-MVS |
| Oxford and Paris [20]       | 2018 | 11       | G    | $\checkmark$            | $\times$     | $\times$     | $\times$          | $\times$   |
| IMC Phototourism [10]       | 2021 | 9        | G    | $\checkmark$            | $\times$     | $\times$     | $\checkmark$      | COLMAP-MVS |
| Graz4K [6]                  | 2026 | 6        | G    | $\checkmark$            | $\checkmark$ | $\checkmark$ | $\checkmark$      | $\times$   |
| <b>TerraSky3D</b>           | 2026 | 155      | M    | $\checkmark/\checkmark$ | $\checkmark$ | $\checkmark$ | $\checkmark$      | APD-MVS    |

stance, the aerial imagery in AerialMegaDepth [29] relies on pseudo-synthetic images rendered from 3D city-wide meshes rather than real photographs, which might introduce a significant domain gap. Similarly, University-1652 [36] provides correspondences between satellite and drone views, yet its drone imagery is synthetic and ground imagery are scraped from Google Street View. In terms of real-world data, Culture3D [35] employs a controlled capture methodology comparable to ours; however, it prioritizes dense coverage of indoor and outdoor scenes for novel view synthesis rather than 3D reconstructions. Furthermore, while the collection process for the Air-to-Ground dataset is described in [3], *only the test set* is publicly available. Finally, CVD-SfM [16] introduces mixed aerial and ground scenes, yet it is restricted to very few scenes. Our dataset addresses these shortcomings by providing a diverse set of high-quality scenes. Specifically, we provide numerous real drone images from aerial perspectives, fully registered within SfM reconstructions alongside ground-level views to ensure cross-domain alignment.

**Stereo Pose Benchmarks.** The IMC Phototourism [10] and MegaDepth-1500 [25] benchmarks, both derived from the MegaDepth dataset, are also widely used for pose estimation and feature matching. However, as they originate from the same source, they inherit the systemic issues discussed in Sec. 2, such as often unreliable intrinsic and extrinsic parameters. Furthermore, the extreme variations in illumination and contrast inherent in these images pose significant challenges for downstream tasks that rely on photometric

consistency or differentiable rendering losses.

A further step toward modern image collection and benchmarking was made with Graz4K [6], an urban 4K dataset collected with pre-calibrated intrinsics and reconstructed with COLMAP. Images were collected in a reduced time span, ensuring consistent lighting conditions and complete view-point coverage. Except for the MegaDepth Air-to-Ground test set [3] and CVD-SfM [16], none of these benchmarks include captured aerial imagery, which is fundamental for testing models in a practical scenario.

### 3. Pipeline

#### 3.1. Data Collection and Scene Diversity

Data are collected primarily using various smartphones for ground capturing and a DJI Mavic 3 drone for aerial ones. For each scene, one to four cameras were used. This device redundancy significantly facilitates robust geometry estimation and allows for more precise intrinsic parameter refinement during bundle adjustment.

The original captures consist of videos at 4K resolution and 30fps, collected across 26 cities in 10 countries, as illustrated in Fig. 2. From the videos, approximately 50,000 images were extracted by uniform sampling. The dataset includes 30 scenes with successfully registered images from both ground-level and aerial perspectives, a combination currently rare in public benchmarks. An additional 5 scenes feature aerial-only footage, while the remaining 115 scenes provide ground-level perspectives. The dataset encompasses



Figure 3. **Example Scene from TerraSky3D.** Left: Sparse reconstruction of the Natural History Museum, Vienna, Austria. Right: The first row shows example images, and the second row shows the corresponding semantically filtered depth maps.

a diverse array of European landmarks and urban environments, including medieval castles, historical buildings, arches, statues, fountains, bridges, dams, piers, shrines, as well as unique viewpoints such as lakeside villas captured from water perspectives. Overall, the dataset provides over 2.5 million image pairs with a global mean reprojection error of only 0.8 pixels.

### 3.2. Geometry Estimation

Despite the recent emergence of several alternatives, including traditional systems such as GLOMAP [19] and FastMap [15], as well as learning-based approaches like VGGT [30], we found COLMAP [23] to remain the most robust and reliable solution for our setting.

We pre-calibrate each camera using a ChArUco board and OpenCV [2], achieving sub-pixel reprojection errors. The resulting intrinsics are stored using the `SIMPLE_RADIAL` model. Finally, after running COLMAP with these pre-calibrated intrinsics, we manually inspect each scene to ensure all cameras are correctly registered and positioned in locations consistent with the corresponding RGB images.

### 3.3. Depth Computation

We utilize Adaptive Patch Deformation MVS (APD-MVS) introduced by Wang et al. [31] to address depth estimation failures in large, textureless regions. Unlike the standard PatchMatch algorithm used in COLMAP (and MegaDepth), which employs a fixed-size square matching window, APD-MVS dynamically adjusts its receptive field achieving state-

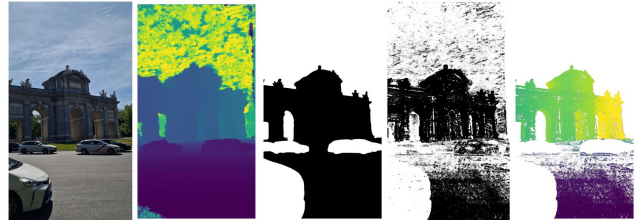


Figure 4. **Visualization of the Depth Filtering Process.** From left to right: original RGB image, raw depth map from APD-MVS, semantic mask, APD-MVS confidence mask, and the filtered depth map. The scene depicted is the Arch of Victory, Madrid, Spain.

of-the-art performance on benchmarks such as ETH3D [24] and Tanks and Temples [13].

To refine the reconstruction in areas that violate MVS assumptions, such as the sky, vegetation, or transient objects, we implement a semantic filtering post-processing step. We employ Mask2Former [4] to segment these regions from the source RGB images, generating a unified binary mask used to prune the resulting depth maps (Fig. 4). Furthermore, we release the original APD-MVS confidence masks to facilitate additional downstream filtering.

### 3.4. Format and Split

For each scene, the dataset provides RGB images organized in camera-specific folders, along with the corresponding COLMAP sparse reconstruction and filtered depth maps.

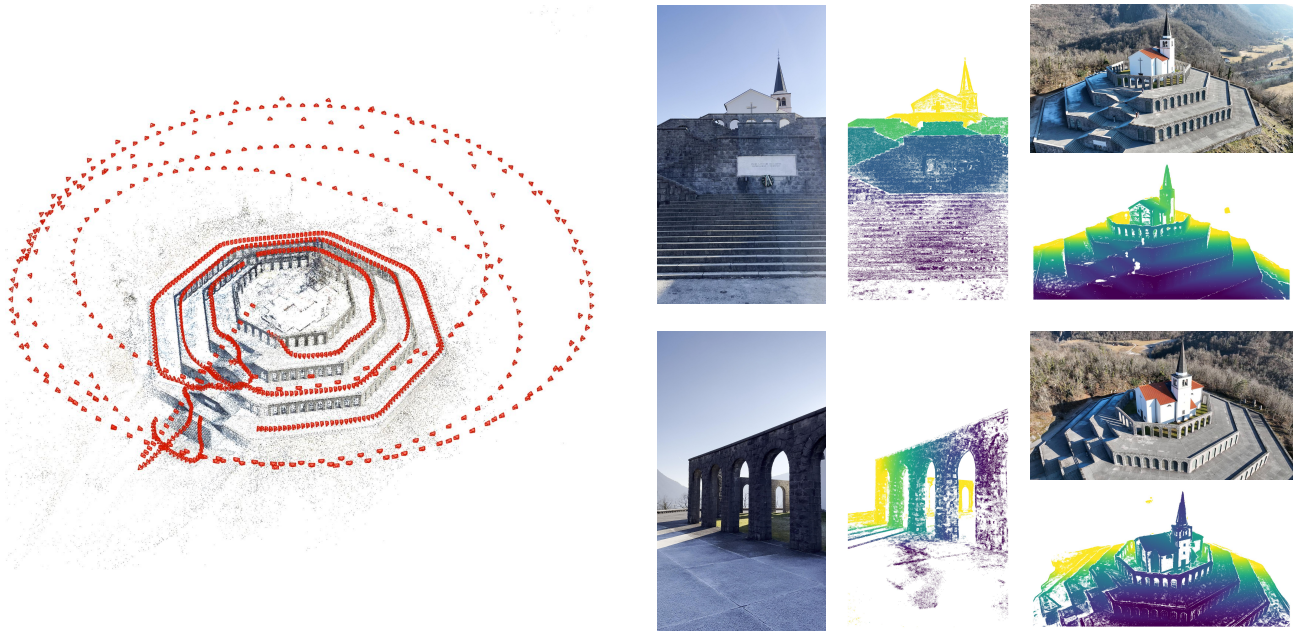


Figure 5. **Example Scene from TerraSky3D.** Left: Sparse reconstruction of the Italian Charnel House, Kobarid, Slovenia. Right: Representative images collected from aerial and ground perspectives, shown with their corresponding semantically filtered depth maps.

While the entire dataset can be utilized for training large-scale models, we propose an official data split to ensure consistent evaluation. Specifically, the scenes listed in the lower section of Tab. 4 are designated as the official test set.

## 4. Experiments

### 4.1. Stereo Pose Estimation

We benchmark state-of-the-art models on our test set to evaluate their performance across modern ground, aerial, and aerial and ground (mixed) scenarios. We consider two different categories of models: deep sparse feature extractors [3, 5–7, 28, 34] and deep matchers [8, 14, 18]. Input images are downsampled to Full HD resolution for the first category and to the optimal resolution indicated by the respective authors for the second. Beginning with the COLMAP matching graph, we first identify image pairs with at least 30 inliers. For pairs within the same category (ground-to-ground or aerial-to-aerial), we discard those with fewer than 100 or more than 500 matches to maintain a balanced graph. In contrast, we retain all valid pairs for the mixed aerial and ground case to ensure sufficient connectivity across viewpoints. The test set comprises a total of over 43,000 pairs distributed as 74.9% ground, 10.7% aerial, and 14.4% mixed. We report performance using the Area Under the Curve (AUC) of the pair-wise pose errors, where the error is defined as the maximum of the rotation error  $\Delta R$  and the translation error  $\Delta t$  as in [6, 7, 18, 34]. We evaluate this up to a threshold of  $5^\circ$ .

Quantitative results are summarized in Tab. 2, categorized

by pair type (e.g., the ground category includes all and only pairs where both images are captured from a ground level). The mean score is computed by averaging the results of all three scenarios with equal weights.

We observe that recent sparse feature extractors exhibit highly similar performance in the *Ground* category, suggesting a plateau in current methodologies or training data. Conversely, the *Aerial* category reveals a broader spectrum of results, indicating that certain methods are better suited for aerial-to-aerial matching. The *Mixed* scenario remains the most challenging due to extreme viewpoint variations, as evidenced by significantly lower scores across all methods. Notably, the combination of ALIKED [34] and SANDesc [6] emerges as the top-performing approach, with a substantial margin in both the *Aerial* and *Mixed* scenarios.

Notably, retraining SANDesc on our TerraSky3D (TS3D) dataset using the original protocol allows the model to cover the traditional ground-level cases found in MegaDepth (MD) while expanding its capabilities to include both aerial-to-aerial and, most importantly, cross-view aerial and ground scenarios. While accuracy remains comparable to the baseline, namely SANDesc (MD), in ground-to-ground and aerial-to-aerial tasks, the model achieves a significant 1.8-point improvement in  $AUC@5^\circ$  within the *Mixed* scenario. This gain showcases the effectiveness of our specialized training data for cross-view tasks.

Although LightGlue [18] achieves performance levels comparable to ALIKED+SANDesc (TS3D), in both *Aerial* and *Mixed* scenarios, deep matchers generally outperform

Table 2. **Relative Pose Estimation Performance on the TerraSky3D Test Set.** We report performance in terms of AUC@5°. The keypoints budget is set to 4096. MD and TS3D denote models trained on MegaDepth and TerraSky3D.

| Method                |                         | AUC@5↑              |             |             |             |
|-----------------------|-------------------------|---------------------|-------------|-------------|-------------|
|                       |                         | Ground              | Aerial      | Mixed       | Mean        |
| Sparse FE             | SuperPoint [5]          | 53.2                | 57.9        | 17.7        | 42.9        |
|                       | DISK [28]               | 56.1                | 72.1        | 29.5        | 52.6        |
|                       | S-TREK [21]             | 62.0                | 81.8        | 36.9        | 60.2        |
|                       | DeDoDe-G [7]            | 62.7                | 78.8        | 35.5        | 59.0        |
|                       | RDD [3]                 | 62.3                | 74.5        | 28.7        | 55.2        |
|                       | ALIKED [34]             | 62.4                | 70.3        | 27.5        | 53.4        |
|                       | ↳ w/ SANDesc [6] (MD)   | 64.2                | 85.6        | 42.9        | 64.2        |
|                       | ↳ w/ SANDesc [6] (TS3D) | <b>64.7</b>         | <b>85.7</b> | <b>44.7</b> | <b>65.0</b> |
|                       | Matchers                | DISK+LightGlue [18] | 68.3        | 85.7        | 44.2        |
| ALIKED+LightGlue [18] |                         | 68.4                | 87.6        | 46.4        | 67.5        |
| MASt3R [14]           |                         | 73.5                | 88.0        | 55.0        | 72.2        |
| RoMa [8]              |                         | <b>77.4</b>         | <b>93.3</b> | <b>75.6</b> | <b>82.1</b> |

sparse methods. MASt3R [14] shows improvements over the LightGlue baselines, while RoMa [8] emerges as the top-performing model across all categories. Its robustness is derived from a dense-warping paradigm rather than the traditional point-to-point matching, yielding up to a 10× increase in inlier counts which significantly stabilizes geometry estimation. However, this superior accuracy entails a notable computational trade-off, as RoMa remains the slowest method among the evaluated suite, both for its size and quadratic cost.

## 4.2. End-to-End 3D Reconstruction

We evaluate three end-to-end learning-based 3D reconstruction pipelines on TerraSky3D, namely VGGT [30],  $\pi^3$  [32], and MapAnything [11]. To evaluate the accuracy of a given method, we measure the relative pose distances within the same scenes. In particular, we compare the ground truth relative transformation between two cameras against the relative transformation predicted by the evaluated model. We define the relative distance error  $E_{rel}$  for every pair of images  $(i, j)$  as follows:

$$E_{rel}(i, j) = \rho \left( (P_i^{gt})^{-1} P_j^{gt}, \hat{P}_i^{-1} \hat{P}_j \right), \quad (1)$$

where  $P^{gt}$  represents the ground truth absolute pose,  $\hat{P}$  represents the estimated absolute pose, and the function  $\rho(\cdot, \cdot)$  computes the maximum of the angular errors in rotation and translation between the two resulting relative transformations. Finally, we report the AUC@5° in Tab. 3.

Our evaluation reveals distinct trade-offs between architectural robustness, and peak precision among the different state-of-the-art models. VGGT [30] emerges as the most consistent performer, achieving the highest mean AUC at 5° of 49.7. Its ability to maintain high scores across diverse geographic locations suggests superior generalization ca-

Table 3. **Absolute Pose Estimation Performance on the TerraSky3D Test Set.** We report performance in terms of AUC@5°. MapAny. stands for MapAnything.

|                          | Imgs | AUC@5↑      |              |              |
|--------------------------|------|-------------|--------------|--------------|
|                          |      | VGGT [30]   | MapAny. [11] | $\pi^3$ [32] |
| Graz Church              | 239  | <b>71.4</b> | 53.7         | 0.0          |
| Graz Townhall            | 335  | 17.9        | <b>51.7</b>  | 26.9         |
| Graz University          | 382  | <b>33.1</b> | 26.4         | 12.0         |
| Munich Frauenkirche      | 123  | 68.2        | 65.2         | <b>77.3</b>  |
| Munich Marienplatz       | 246  | 56.4        | 60.0         | <b>68.5</b>  |
| Munich Theatine Church   | 120  | 67.0        | 49.5         | <b>70.3</b>  |
| Salzburg Andrakirche     | 114  | 70.3        | 44.7         | <b>82.4</b>  |
| Salzburg Rechte Altstadt | 58   | 68.9        | 65.2         | <b>78.5</b>  |
| Udine Devils Bridge      | 339  | <b>37.2</b> | 23.9         | 0.3          |
| Udine Fagagna Church     | 274  | <b>49.8</b> | 40.8         | 0.9          |
| Udine Villalta Castle    | 688  | 0.5         | <b>2.2</b>   | 0.0          |
| Vienna State Opera       | 106  | 55.2        | <b>57.5</b>  | 24.2         |
| Mean                     |      | <b>49.7</b> | 45.0         | 36.8         |

pabilities. In contrast, while  $\pi^3$  [32] achieves the highest individual scores on several scenes, it suffers from catastrophic failures. Specifically, its performance significantly drops in aerial and ground scenarios, indicating geometric instability in these specific wide-baseline scenarios.

## 4.3. Novel View Synthesis

To evaluate Novel View Synthesis (NVS), we establish a benchmark by uniformly sampling 1 every 8 images to create the test set, then we train 3D Gaussian Splatting (3DGS) [12] on the remains images for 30,000 iterations.

Tab. 4 reports the evaluation of the synthesized novel views in terms of Learned Perceptual Image Patch Similarity (LPIPS) [33], Peak Signal-to-Noise Ratio (PSNR), and Structural Similarity Index Measure (SSIM). LPIPS assesses perceptual similarity, where lower scores correspond to better visual alignment with human perception. Conversely, for PSNR and SSIM, higher scores indicate superior reconstruction quality and structural fidelity.

## 4.4. Bidirectional Geometric Consistency

To evaluate our depth maps, we perform a bidirectional reprojection consistency check. We utilize the COLMAP viewgraphs to select image pairs  $(I_i, I_j)$  with at least 100 matches. For each pair, we verify consistency by computing the cyclic reprojection error. Let  $\mathbf{p}_i$  be a pixel coordinate in image  $I_i$ . We first unproject  $\mathbf{p}_i$  to 3D space using its estimated depth  $D_i(\mathbf{p}_i)$  and project it into the view of  $I_j$  to obtain the coordinate  $\mathbf{p}_{i \rightarrow j}$ . We then sample the depth  $D_j$  at this new location to project back into the original frame  $I_i$ , resulting in the coordinate  $\mathbf{p}_{i \rightarrow j \rightarrow i}$ . The cyclic error is defined as the Euclidean distance:

$$E_{cyc}(\mathbf{p}_i) = \|\mathbf{p}_i - \mathbf{p}_{i \rightarrow j \rightarrow i}\|_2 \quad (2)$$

We run the consistency checks in both directions, i.e.,  $I_i \rightarrow I_j$  and  $I_j \rightarrow I_i$ . To include all mixed aerial and ground pairs

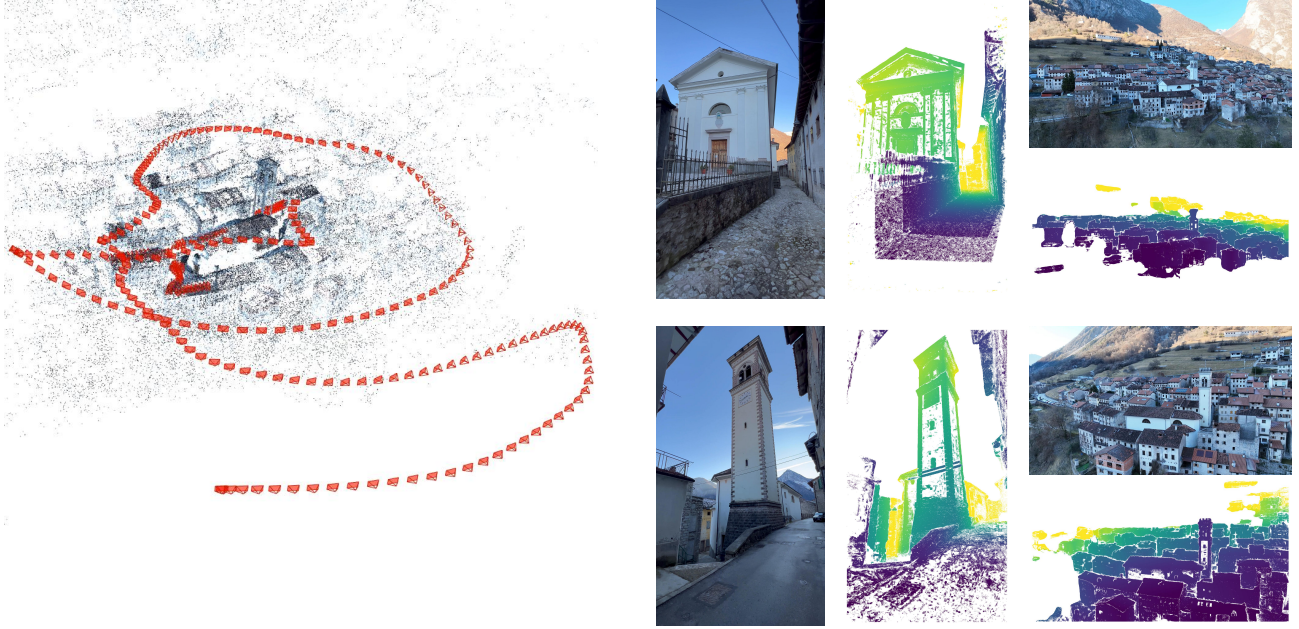


Figure 6. **Example Scene from TerraSky3D.** Left: Sparse reconstruction of Erto e Casso, Pordenone, Italy. Right: Representative images collected from aerial and ground perspectives, shown with their corresponding semantically filtered depth maps.

Table 4. **NVS Benchmark Results on TerraSky3D.** Scene types are G (Ground), A (Aerial), and M (Mixed Aerial and Ground).

|              | Scene                         | Type | PSNR $\uparrow$ | SSIM $\uparrow$ | LPIPS $\downarrow$ |
|--------------|-------------------------------|------|-----------------|-----------------|--------------------|
| Training set | Trieste Unity Square          | G    | 22.21           | 0.759           | 0.318              |
|              | Vienna Natural History Museum | G    | 21.92           | 0.754           | 0.342              |
|              | Udine Abandoned Bridge        | A    | 21.73           | 0.625           | 0.326              |
|              | Gorizia Military Shrine       | M    | 21.53           | 0.656           | 0.398              |
|              | Udine Villalta Church         | M    | 23.76           | 0.746           | 0.302              |
| Test set     | Graz Church                   | G    | 22.39           | 0.801           | 0.197              |
|              | Graz Townhall                 | G    | 21.54           | 0.733           | 0.266              |
|              | Graz University               | G    | 24.40           | 0.821           | 0.233              |
|              | Munich Frauenkirche           | G    | 21.12           | 0.728           | 0.250              |
|              | Munich Marienplatz            | G    | 19.38           | 0.708           | 0.323              |
|              | Munich Theatine Church        | G    | 21.53           | 0.799           | 0.225              |
|              | Salzburg Andrakirche          | G    | 21.32           | 0.811           | 0.222              |
|              | Salzburg Rechte Altstadt      | G    | 21.56           | 0.856           | 0.186              |
|              | Udine Devils Bridge           | M    | 23.27           | 0.748           | 0.324              |
|              | Udine Fagagna Church          | M    | 21.02           | 0.639           | 0.361              |
|              | Udine Villalta Castle         | M    | 19.95           | 0.529           | 0.488              |
|              | Vienna State Opera            | G    | 22.33           | 0.826           | 0.230              |

we perform this check across all possible image pairs. The evaluation considers only *valid* pixels. A pixel  $\mathbf{p}_i$  is said *valid* if its projection falls within the image bounds.

We compare TerraSky3D with MegaDepth in terms of both scale and scope. To ensure a fair comparison, we down-scale our 4K resolution images to a resolution of 1,600 pixels on the longest edge. We evaluate both datasets on their respective test sets, as these consist of scenes processed via the same pipeline as the training data, thereby accurately reflecting overall dataset characteristics. Specifically, for the MegaDepth [17] comparison, we focus on the IMC Photo-

Table 5. **Bidirectional Geometric Consistency on TerraSky3D.** We report performance in terms of cumulative inlier percentage under varying pixel error thresholds.

| Scene      | Type                     | Pairs    | Inliers (%) |             |             |             |             |
|------------|--------------------------|----------|-------------|-------------|-------------|-------------|-------------|
|            |                          |          | 1px         | 3px         | 5px         | 10px        |             |
| MegaDepth  | British Museum           | G        | 4104        | 39.0        | 51.3        | 53.4        | 54.9        |
|            | Florence Cathedral Side  | G        | 4134        | 47.8        | 62.3        | 65.3        | 67.7        |
|            | Lincoln Memorial Statue  | G        | 3195        | 36.6        | 56.4        | 62.7        | 67.9        |
|            | London Bridge            | G        | 2200        | 42.1        | 56.1        | 60.5        | 65.0        |
|            | Milan Cathedral          | G        | 4279        | 50.6        | 64.5        | 67.9        | 70.8        |
|            | Mount Rushmore           | G        | 4018        | 71.7        | 77.3        | 78.0        | 78.5        |
|            | Piazza San Marco         | G        | 2188        | 53.1        | 69.6        | 73.7        | 77.0        |
|            | Reichstag                | G        | 2116        | 33.8        | 44.0        | 46.7        | 48.9        |
|            | Sacre Coeur              | G        | 3060        | 24.3        | 32.8        | 35.5        | 38.4        |
|            | Sagrada Familia          | G        | 3550        | 39.8        | 58.5        | 63.5        | 67.7        |
|            | St Pauls Cathedral       | G        | 3267        | 40.9        | 58.5        | 63.5        | 67.8        |
|            | St Peters Square         | G        | 2915        | 36.7        | 50.1        | 53.7        | 56.9        |
|            | <b>Mean</b>              | <b>G</b> | <b>3252</b> | <b>43.0</b> | <b>56.8</b> | <b>60.4</b> | <b>63.4</b> |
| TerraSky3D | Graz Church              | G        | 12736       | 35.3        | 56.9        | 66.1        | 76.0        |
|            | Graz Townhall            | G        | 9556        | 40.0        | 59.4        | 67.7        | 77.0        |
|            | Graz University          | G        | 9792        | 59.6        | 74.5        | 78.7        | 82.4        |
|            | Munich Frauenkirche      | G        | 2446        | 63.4        | 81.1        | 85.6        | 89.3        |
|            | Munich Marienplatz       | G        | 5821        | 48.6        | 61.9        | 66.3        | 70.9        |
|            | Munich Theatine Church   | G        | 2617        | 60.8        | 77.1        | 81.3        | 85.0        |
|            | Salzburg Andrakirche     | G        | 3085        | 41.7        | 57.2        | 61.8        | 66.0        |
|            | Salzburg Rechte Altstadt | G        | 1039        | 62.4        | 74.6        | 77.7        | 80.5        |
|            | Udine Devils Bridge      | M        | 9569        | 43.7        | 57.2        | 61.3        | 65.4        |
|            | Udine Fagagna Church     | M        | 3848        | 56.1        | 67.6        | 70.3        | 72.9        |
|            | Udine Villalta Castle    | M        | 9023        | 51.4        | 64.5        | 68.5        | 72.3        |
|            | Vienna State Opera       | G        | 2310        | 54.0        | 67.9        | 71.8        | 75.5        |
|            | <b>Mean</b>              | <b>M</b> | <b>5986</b> | <b>51.4</b> | <b>66.7</b> | <b>71.4</b> | <b>76.1</b> |

tourism [10] test set, as it constitutes a representative subset of the larger MegaDepth collection.

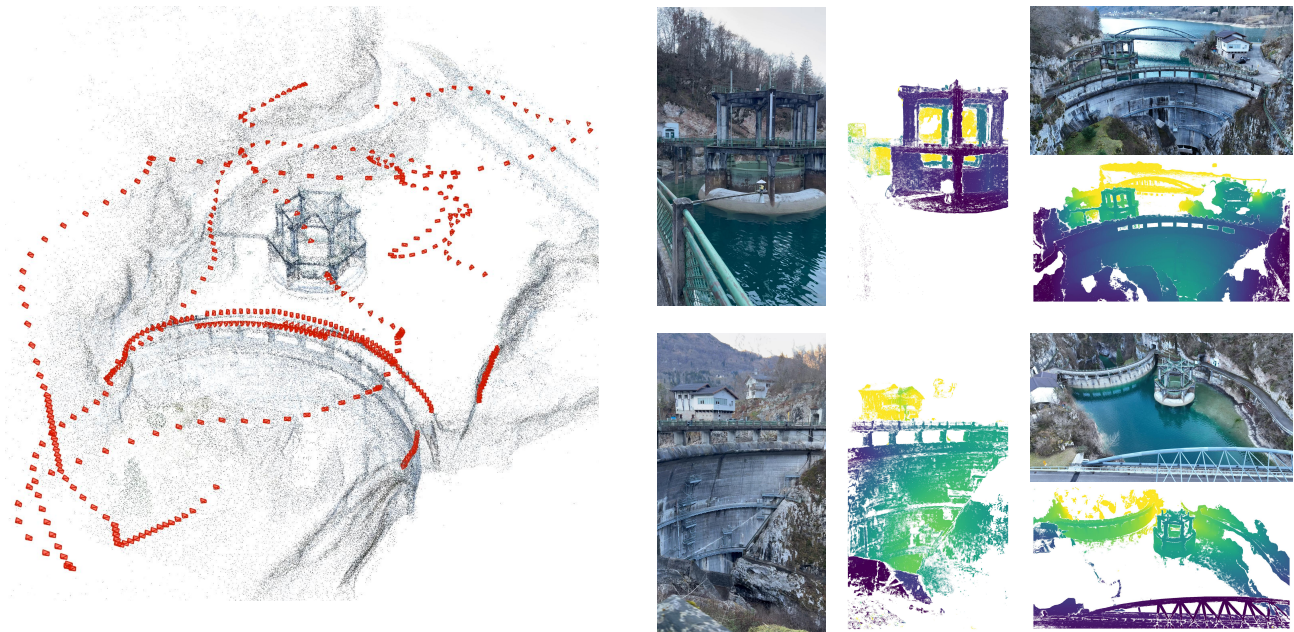


Figure 7. **Example Scene from TerraSky3D.** Left: Sparse reconstruction of the Barcis Dam, Pordenone, Italy. Right: Representative images collected from aerial and ground perspectives, shown with their corresponding semantically filtered depth maps.

Tab. 5 reports the percentage of *valid* pixels at cumulative thresholds demonstrating that our data exhibits higher geometric consistency across all error thresholds. It is important to note that even a small percentage-wise improvement represents thousands of additional valid points that can be used in training or evaluation tasks. Furthermore, our dataset includes aerial and ground image pairs, a challenging cross-modal scenario absent in MegaDepth.

## 5. Limitations

While TerraSky3D significantly expands the availability of public data by introducing complex aerial and ground scenes, it is nonetheless subject to specific technical limitations. Unlike datasets that rely on rendered synthetic frames, our dataset is grounded in raw photographs extracted from high-resolution video sequences. While this ensures real-world authenticity, it introduces unique challenges inherent to physical capture environments.

First, although the source sequences are high-definition, certain frames suffer from motion blur. This phenomenon is particularly pronounced during rapid camera movements or in low-light conditions.

Furthermore, while we implement a robust automated filtering pipeline to uphold data integrity, occasionally the resulting depth maps and associated masks might be imprecise. In complex scenes with intricate geometry, automated processes may struggle to precisely delineate fine-grained boundaries, thin structures, or transparent surfaces.

Finally, depth estimation quality is tied to angular variety

and viewpoint density. To mitigate noise and structural incompleteness in regions with sparse multi-view coverage, we provide APD-MVS confidence masks. This allows users to perform further filtering to maintain higher structural fidelity and visual clarity.

## 6. Conclusion

We introduce **TerraSky3D**, a novel high-quality dataset comprising approximately 50,000 4K images, along with their corresponding sparse 3D reconstructions and depth maps. We address a critical gap in the literature by providing several scenes integrating aerial and ground-level perspectives, a modality essential for advancing the state of the art in cross-view localization and reconstruction.

In particular, we show, that most current state-of-the-art models struggle in aerial and mixed scenarios, thus limiting their effectiveness in practical applications. Nevertheless, a SANDesc model retrained on our data outperforms the original model trained on MegaDepth. Ultimately, TerraSky3D provides a robust foundation for future research in large-scale 3D computer vision.

**Acknowledgements** We thank Davide Casano, Luca Danellutti, Federico Fattori, Alessandro Menafra, Florian Thaler, Runze Yuan, and Stefano Zorzi for their contribution in data collection.

This work has been supported by the FFG under Contract No. 881844 within the project “Pro<sup>2</sup>Future”.

## References

- [1] Vassileios Balntas, Karel Lenc, Andrea Vedaldi, and Krystian Mikolajczyk. HPatches: A benchmark and evaluation of handcrafted and learned local descriptors. In *Proceedings of the IEEE Conference on Computer Vision and Pattern Recognition (CVPR)*, pages 5173–5182. IEEE, 2017. 3
- [2] Gary Bradski, Adrian Kaehler, et al. Opencv. *Dr. Dobbs's journal of software tools*, 3(2), 2000. 4
- [3] Gonglin Chen, Tianwen Fu, Haiwei Chen, Wenbin Teng, Hanyuan Xiao, and Yajie Zhao. Rdd: Robust feature detector and descriptor using deformable transformer. In *Proceedings of the Computer Vision and Pattern Recognition Conference*, pages 6394–6403, 2025. 2, 3, 5, 6
- [4] Bowen Cheng, Ishan Misra, Alexander G Schwing, Alexander Kirillov, and Rohit Girdhar. Masked-attention mask transformer for universal image segmentation. In *Proceedings of the IEEE/CVF Conference on Computer Vision and Pattern Recognition (CVPR)*, pages 1290–1300, 2022. 4
- [5] Daniel DeTone, Tomasz Malisiewicz, and Andrew Rabinovich. Superpoint: Self-supervised interest point detection and description. In *Proceedings of the IEEE conference on computer vision and pattern recognition workshops*, pages 224–236, 2018. 5, 6
- [6] Mattia D'Urso, Emanuele Santellani, Christian Sormann, Mattia Rossi, Andreas Kuhn, and Friedrich Fraundorfer. A streamlined attention-based network for descriptor extraction. In *2026 International Conference on 3D Vision (3DV)*. IEEE Computer Society, 2026. 3, 5, 6
- [7] Johan Edstedt, Georg Bökman, Mårten Wadenbäck, and Michael Felsberg. Dedode: Detect, don't describe—describe, don't detect for local feature matching. *arXiv preprint arXiv:2308.08479*, 2023. 5, 6
- [8] Johan Edstedt, Qiyu Sun, Georg Bökman, Mårten Wadenbäck, and Michael Felsberg. Roma: Robust dense feature matching. In *Proceedings of the IEEE/CVF Conference on Computer Vision and Pattern Recognition*, pages 19790–19800, 2024. 5, 6
- [9] Johan Edstedt, David Nordström, Yushan Zhang, Georg Bökman, Jonathan Astermark, Viktor Larsson, Anders Heyden, Fredrik Kahl, Mårten Wadenbäck, and Michael Felsberg. Roma v2: Harder better faster denser feature matching. *arXiv preprint arXiv:2511.15706*, 2025. 2
- [10] Yuhe Jin, Dmytro Mishkin, Anastasiia Mishchuk, Jiri Matas, Pascal Fua, Kwang Moo Yi, and Eduard Trulls. Image matching across wide baselines: From paper to practice. *International Journal of Computer Vision*, 129(2):517–547, 2021. 2, 3, 7
- [11] Nikhil Keetha, Norman Müller, Johannes Schönberger, Lorenzo Porzi, Yuchen Zhang, Tobias Fischer, Arno Knapitsch, Duncan Zauss, Ethan Weber, Nelson Antunes, et al. Mapanything: Universal feed-forward metric 3d reconstruction. *arXiv preprint arXiv:2509.13414*, 2025. 6
- [12] Bernhard Kerbl, Georgios Kopanas, Thomas Leimkühler, and George Drettakis. 3d gaussian splatting for real-time radiance field rendering. *ACM Transactions on Graphics*, 42(4), 2023. 6
- [13] Arno Knapitsch, Jaesik Park, Qian-Yi Zhou, and Vladlen Koltun. Tanks and temples: Benchmarking large-scale scene reconstruction. *ACM Transactions on Graphics*, 36(4), 2017. 4
- [14] Vincent Leroy, Yohann Cabon, and Jérôme Revaud. Grounding image matching in 3d with mast3r. In *European Conference on Computer Vision*, pages 71–91. Springer, 2024. 5, 6
- [15] Jiahao Li, Haochen Wang, Muhammad Zubair Irshad, Igor Vasiljevic, Matthew R Walter, Vitor Campagnolo Guizilini, and Greg Shakhnarovich. Fastmap: Revisiting dense and scalable structure from motion. *arXiv preprint arXiv:2505.04612*, 2025. 4
- [16] Yaxuan Li, Yewei Huang, Bijay Gaudel, Hamidreza Jafarnejadsani, and Brendan Englot. Cvd-sfm: A cross-view deep front-end structure-from-motion system for sparse localization in multi-altitude scenes. *arXiv preprint arXiv:2508.01936*, 2025. 2, 3
- [17] Zhengqi Li and Noah Snavely. Megadepth: Learning single-view depth prediction from internet photos. In *Proceedings of the IEEE conference on computer vision and pattern recognition*, pages 2041–2050, 2018. 1, 2, 3, 7
- [18] Philipp Lindenberger, Paul-Edouard Sarlin, and Marc Pollefeys. Lightglue: Local feature matching at light speed. In *Proceedings of the IEEE/CVF international conference on computer vision*, pages 17627–17638, 2023. 5, 6
- [19] Linfei Pan, Dániel Baráth, Marc Pollefeys, and Johannes L Schönberger. Global structure-from-motion revisited. In *European Conference on Computer Vision*, pages 58–77. Springer, 2024. 4
- [20] Filip Radenović, Ahmet Iscen, Giorgos Tolias, Yannis Avrithis, and Ondřej Chum. Revisiting oxford and paris: Large-scale image retrieval benchmarking. In *Proceedings of the IEEE conference on computer vision and pattern recognition*, pages 5706–5715, 2018. 3
- [21] Emanuele Santellani, Christian Sormann, Mattia Rossi, Andreas Kuhn, and Friedrich Fraundorfer. S-trek: Sequential translation and rotation equivariant keypoints for local feature extraction. In *Proceedings of the IEEE/CVF International Conference on Computer Vision*, pages 9728–9737, 2023. 6
- [22] Torsten Sattler, Will Maddern, Carl Toft, Akihiko Torii, Lars Hammarstrand, Erik Stenborg, Daniel Safari, Masatoshi Okutomi, Marc Pollefeys, Josef Sivic, et al. Benchmarking 6dof outdoor visual localization in changing conditions. In *Proceedings of the IEEE conference on computer vision and pattern recognition*, pages 8601–8610, 2018. 3
- [23] Johannes L Schönberger and Jan-Michael Frahm. Structure-from-motion revisited. In *Proceedings of the IEEE conference on computer vision and pattern recognition*, pages 4104–4113, 2016. 2, 4
- [24] Thomas Schops, Johannes L Schönberger, Silvano Galliani, Torsten Sattler, Konrad Schindler, Marc Pollefeys, and Andreas Geiger. A multi-view stereo benchmark with high-resolution images and multi-camera videos. In *Proceedings of the IEEE conference on computer vision and pattern recognition*, pages 3260–3269, 2017. 2, 4
- [25] Jiaming Sun, Zehong Shen, Yuang Wang, Hujun Bao, and Xiaowei Zhou. Loftr: Detector-free local feature matching with

- transformers. In *Proceedings of the IEEE/CVF conference on computer vision and pattern recognition*, pages 8922–8931, 2021. 3
- [26] Akihiko Torii, Relja Arandjelovic, Josef Sivic, Masatoshi Okutomi, and Tomas Pajdla. 24/7 place recognition by view synthesis. In *Proceedings of the IEEE conference on computer vision and pattern recognition*, pages 1808–1817, 2015. 3
- [27] Joseph Tung, Gene Chou, Ruojin Cai, Guandao Yang, Kai Zhang, Gordon Wetzstein, Bharath Hariharan, and Noah Snavely. Megascenes: Scene-level view synthesis at scale. In *ECCV*, 2024. 1, 2, 3
- [28] Michał Tyszkiewicz, Pascal Fua, and Eduard Trulls. Disk: Learning local features with policy gradient. *Advances in neural information processing systems*, 33:14254–14265, 2020. 5, 6
- [29] Khiem Vuong, Anurag Ghosh, Deva Ramanan, Srinivasa Narasimhan, and Shubham Tulsiani. Aerialmegadepth: Learning aerial-ground reconstruction and view synthesis. In *Proceedings of the Computer Vision and Pattern Recognition Conference*, pages 21674–21684, 2025. 2, 3
- [30] Jianyuan Wang, Minghao Chen, Nikita Karaev, Andrea Vedaldi, Christian Rupprecht, and David Novotny. Vggt: Visual geometry grounded transformer. In *Proceedings of the Computer Vision and Pattern Recognition Conference*, pages 5294–5306, 2025. 4, 6
- [31] Yuesong Wang, Zhaojie Zeng, Tao Guan, Wei Yang, Zhuo Chen, Wenkai Liu, Luoyuan Xu, and Yawei Luo. Adaptive patch deformation for textureless-resilient multi-view stereo. In *Proceedings of the IEEE/CVF Conference on Computer Vision and Pattern Recognition (CVPR)*, pages 1621–1630, 2023. 2, 4
- [32] Yifan Wang, Jianjun Zhou, Haoyi Zhu, Wenzheng Chang, Yang Zhou, Zizun Li, Junyi Chen, Jiangmiao Pang, Chunhua Shen, and Tong He.  $\pi^3$ : Permutation-equivariant visual geometry learning. *arXiv preprint arXiv:2507.13347*, 2025. 6
- [33] Richard Zhang, Phillip Isola, Alexei A Efros, Eli Shechtman, and Oliver Wang. The unreasonable effectiveness of deep features as a perceptual metric. In *Proceedings of the IEEE conference on computer vision and pattern recognition*, pages 586–595, 2018. 6
- [34] Xiaoming Zhao, Xingming Wu, Weihai Chen, Peter CY Chen, Qingsong Xu, and Zhengguo Li. Aliked: A lighter keypoint and descriptor extraction network via deformable transformation. *IEEE Transactions on Instrumentation and Measurement*, 72:1–16, 2023. 5, 6
- [35] Xinyi Zheng, Steve Zhang, Weizhe Lin, Aaron Zhang, Walterio W Mayol-Cuevas, and Junxiao Shen. Culture3d: Cultural landmarks and terrain dataset for 3d applications. *arXiv preprint arXiv:2501.06927*, 2025. 2, 3
- [36] Zhedong Zheng, Yunchao Wei, and Yi Yang. University-1652: A multi-view multi-source benchmark for drone-based geolocalization. In *Proceedings of the 28th ACM international conference on Multimedia*, pages 1395–1403, 2020. 2, 3